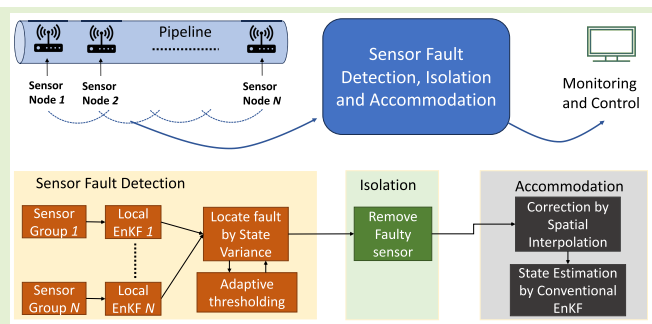


Model-Based Architecture for Multisensor Fault Detection, Isolation, and Accommodation in Natural-Gas Pipelines

Khadija Shaheen¹, Member, IEEE, Apoorva Chawla, Member, IEEE, Ferdinand Evert Uilhoorn², and Pierluigi Salvo Rossi³, Senior Member, IEEE

Abstract—A significant quantity of sensors distributed throughout the natural gas pipeline is susceptible to errors. Timely diagnosis of sensor faults in such scenarios holds great significance in averting catastrophic failures. This article proposes a novel approach termed model-based multisensor fault detection, isolation, and accommodation (MM-SFDIA) technique to mitigate multiple sensor faults occurring simultaneously in large-scale distributed systems. The proposed approach leverages a distributed filtering framework, employing multiple local ensemble Kalman filters (EnKFs). Each individual local filter generates a distinct local state estimation using a distinct set of sensor measurements. By analyzing the differences among these local state estimates, a strategy based on state consistency, the faulty sensors are identified. Furthermore, an adaptive thresholding technique is devised to ensure resilient fault detection and identification. Compared with the existing state-of-the-art techniques, the proposed approach offers a lower computational burden and is applicable to high-dimensional nonlinear systems with numerous sensor faults. Moreover, the results affirm the effectiveness of the proposed architecture, demonstrating a high accuracy and low execution time in detecting and isolating multiple sensor faults.

Index Terms—Adaptive threshold, data fusion, ensemble Kalman filter (EnKF), fault diagnosis, model-based technique, multiple sensor faults, natural-gas pipelines, transient flow.



I. INTRODUCTION

TIMELY monitoring of natural-gas pipelines is crucial to ensure the safety and reliability of the overall system. With the advancements in digital technologies, several urban gas pipeline monitoring systems have been developed to detect potential leaks [1], [2]. These systems typically employ

Manuscript received 29 November 2023; accepted 15 December 2023. Date of publication 27 December 2023; date of current version 31 January 2024. This work was supported in part by the Research Council of Norway through the Project SIGNIFY within the IKTPLUSS Framework under Grant 311902. The associate editor coordinating the review of this article and approving it for publication was Dr. Pedro Oliveira Conceição Junior. (Corresponding author: Khadija Shaheen.)

Khadija Shaheen and Apoorva Chawla are with the Department of Electronic Systems, Norwegian University of Science and Technology, 7491 Trondheim, Norway (e-mail: shaheen.khadija@ntnu.no; apoorva.chawla@ntnu.no).

Ferdinand Evert Uilhoorn is with the Department of Gas Engineering, Warsaw University of Technology, 00-653 Warsaw, Poland (e-mail: ferdinand.uilhoorn@pw.edu.pl).

Pierluigi Salvo Rossi is with the Department of Electronic Systems, Norwegian University of Science and Technology, 7491 Trondheim, Norway, and also with the Department of Gas Technology, SINTEF Energy Research, 7491 Trondheim, Norway (e-mail: salvorossi@ieee.org).

Digital Object Identifier 10.1109/JSEN.2023.3345004

different types of gas-monitoring sensors to continuously monitor gas pipelines and promptly detect leaks or potential issues, thus enhancing the overall security and reliability of the pipeline infrastructure. However, the sensors installed in the pipelines might be faulty (e.g., due to harsh environmental conditions) with incorrect sensor readings and delayed/missed leak detection resulting potentially in catastrophic failures. Consequently, it is crucial to develop effective techniques for timely fault diagnosis in gas-monitoring systems.

Several approaches, including manual analysis methods, signals processing-based methods, model-based methods, and data-driven methods, can be employed to facilitate sensor fault detection in natural-gas pipelines. Manual analysis diagnostic approaches are often inaccurate and time-consuming; conversely, fault diagnosis based on data-driven approaches has been widely used for early sensor-fault detection due to its high capabilities for information processing and complex-data representation [3], [4], [5], [6]. However, data-driven techniques necessitate substantial volumes of data for training and might be unsuitable for online implementation in large-size systems. Differently, methods based on signal-processing techniques are likely lighter to implement and easier to

interpret, but are significantly impacted by background noise and heavily rely on specialized domain expertise, thus still exhibiting relevant challenges to guarantee the accuracy of real-time fault diagnosis [7].

The adoption of model-based techniques for fault diagnosis has gained significant attention, since they are not limited by data availability: if the system model is sufficiently accurate, these techniques exhibit interesting scaling and generalization capabilities. Model-based approaches operate by analyzing the residual signal, which represents the disparity between a computational model and real-world measurements. Among model-based techniques, observer-based methods are predominantly preferred due to their effectiveness and theoretical advantages [8]. These methods estimate the system outputs by employing an observer that is resilient against model uncertainty and interruptions. The most efficient observer-based technique is the Kalman filter, although its application is confined to linear systems. For nonlinear systems, several different variants of the Kalman filter have been proposed, including the extended Kalman filter (EKF) [9], the unscented Kalman filter (UKF) [10], the ensemble Kalman filter (EnKF) [11], and the cubature Kalman filter (CKF) [12].

In general, centralized and distributed data-fusion architectures based on Kalman filters (or different variants) are utilized to facilitate fault diagnosis in large-scale distributed plants with numerous interconnected subsystems. Centralized structures provide high accuracy; however, its significant computing costs may prevent real-time implementation, particularly when dealing with a large number of sensors [10], [21], [22]. In contrast, distributed architectures operate by employing several local filters that work in parallel and subsequently combine their respective outputs through a master filter. This approach enhances decision-making capabilities while reducing the overall computational load [23], [24], [25], [26].

Distributed and centralized multisensor integration architectures based on adaptive EKF data fusion techniques are discussed in [13] for sensor and process fault diagnosis: 1) the centralized architecture, where a single filter combines data from various sensors and exhibits high estimation accuracy, but less resilience to sensor faults and 2) conversely, the distributed architecture, characterized by a collection of local filters (one for each sensor), exhibits limitations in detecting multiple sensor faults and handling substantial nonlinearity. Furthermore, multisensor data fusion techniques for identifying both hardware and software faults are investigated in [14], [15], and [27]. These methodologies adopt a redundancy-based strategy (duplication/comparison) for fault diagnosis, where two sensors collaborate to estimate a single parameter. However, these techniques are only applicable to a single-fault scenario, and the complexity notably escalates while dealing with scenarios involving multiple faults. A fusion technique based on Wasserstein average-consensus classification to handle faulty sensors is proposed in [28]. In this approach, local filters exchange information with neighboring filters and employ clustering algorithms to distinguish between trusted and untrusted local estimates. However, this method is confined to linear systems and needs at least half of the sensors being trustworthy. In [16], a sensor-fusion approach, involving

several Kalman filters (each customized for a specific defect), is designed for nonlinear systems; nevertheless, this method exhibits substantial computational cost restrictions. In [17], a sensor-fusion technique utilizing UKF is investigated for the monitoring of a gas turbine engine: four distinct local filter combinations are considered (corresponding to the sensors installed on the gas turbine); nonetheless, this method lacks the ability to generalize and struggles to accurately isolate the faulty sensors. Similarly, a sensor-fusion system based on UKF is developed in [18] for applications within microgrids, where the number of local filters can be adjusted to accommodate any quantity of sensors; however, the approach solely addresses a single-fault scenario and demonstrates elevated computational costs for multiple fault scenarios.

Most of the existing state-of-the-art techniques primarily focus on single-fault scenarios, while their computation complexity significantly increases when addressing multiple sensor faults. In addition, these techniques hinge on basic models that fall short of capturing the wide spectrum of large-scale dynamics evident in complex real-world processes. When applied to highly nonlinear, complex, and large-scale systems, these approaches entail significant computational costs. Hence, it is crucial to develop a multisensor fault detection framework that is capable of efficiently handling multiple sensor faults in highly nonlinear, complex, and large-scale systems while ensuring minimal computational complexity.

To address these issues, we propose a novel architecture, termed model-based multisensor fault detection, isolation, and accommodation (MM-SFDIA), tailored for natural gas pipelines. The MM-SFDIA approach capitalizes on a distributed filtering structure employing a bank of EnKFs, where each local EnKF utilizes a distinct set of measurements to yield an independent local state estimate. The architecture employs a state coherence strategy that evaluates disparities among the independent local state vector estimations to diagnose faults: during fault-free scenarios, the local state estimates exhibit consistency; conversely, in the presence of a fault, the estimates display high state-variance values. To enhance the accuracy of fault detection, we have also devised a novel adaptive thresholding method that dynamically adjusts the threshold value based on the evolving system conditions. Upon identifying the faulty sensors based on the thresholding technique, the erroneous measurements are substituted with accurately estimated values achieved via spatial interpolation of nonfaulty sensor measurements. In addition, the performance of the proposed architecture is evaluated by employing simulated nonlinear spatiotemporal data combined with synthetically generated faults, specifically bias faults and drift faults. The results demonstrate that the proposed approach exhibits both swift computational speed and remarkable accuracy, even when dealing with weak faults.

In our previous works [19], [20], we presented a model-based SFDIA framework for natural-gas pipelines using the technique outlined in [18]; however, it predominantly focused on addressing single-sensor faults and exhibited considerable computational overhead when confronted with multiple-sensor faults. Differently, the newly proposed MM-SFDIA architecture demonstrates reduced computational

TABLE I
COMPARISON OF THE PROPOSED SCHEME WITH THE EXISTING WORKS ON SENSOR FAULT DIAGNOSIS

Works	Multiple faults	Adaptive thresholding	Filter type	Computation complexity	Applications	Large-scale system	Non-linearity	State consistency	Random weak faults
[13]	✗	✗	EKF	↑ High	Continuous stirred tank reactor	✗	↓ Low	✗	✗
[14], [15]	✗	✗	KF	↑ High	Navigation system	✗	↓ Low	✗	✗
[16]	✗	✗	KF	↑ High	Navigation system	✗	↓ Low	✗	✓
[17]	✗	✗	EKF, UKF	↑ High	Gas turbine engine	✗	↓ Low	✓	✓
[18]	✗	✗	UKF	↑ High	Micro grid	✗	↓ Low	✓	✗
[19]	✗	✗	UKF	↑ High	Natural gas pipeline	✓	↑ High	✓	✓
[20]	✗	✗	EKF,EnKF,UKF	↑ High	Natural gas pipeline	✓	↑ High	✓	✓
Proposed	✓	✓	EnKF	↓ Low	Natural gas pipeline	✓	↑ High	✓	✓

complexity in scenarios involving multiple sensor faults. More specifically, it effectively handles simultaneous multiple sensor faults in highly large-scale, nonlinear, and complex systems by employing an architecture featuring a predetermined number of local filters; thus, it can be applied to diverse systems encompassing any combination of sensors and faults while requiring an exceptionally low-computational cost. Furthermore, we introduce a novel adaptive thresholding technique that substantially enhances the detection performance. Our proposed architecture optimizes the utilization of EnKF, notably reducing computational complexity while achieving high estimation and detection performance in large-scale systems.

Table I furnishes a comparative summary of the proposed approach in contrast to relevant existing state-of-the-art fault diagnosis techniques. The primary contributions of this article are succinctly outlined below.

- 1) A novel model-based architecture is proposed for addressing simultaneous multiple faults in natural gas pipelines experiencing transient flow. The proposed architecture leverages the benefits of the distributed EnKF-based filtering framework and state consistency strategy to effectively handle simultaneous multiple sensor faults in large-scale distributed systems.
- 2) The detection technique, based on state coherence, utilizes local state variance to assess differences among independent estimations of the local state vectors.
- 3) To improve fault detection accuracy, we have developed an innovative adaptive thresholding technique that dynamically adapts the threshold value according to the changing system conditions.
- 4) The fault accommodation is performed by substituting inaccurate measurements with estimated values from reliable sensor data through spatial interpolation.
- 5) A transient flow model is thoroughly discussed accompanied by its numerical solution and emphasis on its application in fault diagnosis.

The rest of this article is outlined as follows. Section II discusses the transient flow model, and Section III presents the proposed MM-SFDIA architecture along with the adaptive thresholding technique. The simulation results to validate the performance of the proposed MM-SFDIA architecture are analyzed in Section IV. Finally, Section V provides some concluding remarks and future directions.

II. TRANSIENT-FLOW MODEL

A. Partial Differential Equations

The system of the first-order quasilinear nonhomogeneous hyperbolic partial differential equations (PDEs) can accurately model the transient flow of natural gas in pipelines [29]. Based on the fundamental principles of mass, momentum, and energy conservation, the system of PDEs can be mathematically represented as follows:

$$\frac{\partial \rho}{\partial t} + \frac{\partial}{\partial s}(\rho v) = 0 \quad (1)$$

$$\rho \frac{\partial v}{\partial t} + \frac{\partial p}{\partial s} + \rho v \frac{\partial v}{\partial s} = -\frac{w}{A} - \rho g \sin \theta \quad (2)$$

$$\rho \left(\frac{\partial h}{\partial t} + v \frac{\partial h}{\partial s} \right) - \frac{\partial p}{\partial t} - v \frac{\partial p}{\partial s} = \frac{q + wv}{A}. \quad (3)$$

Here, the variables A , v , ρ , p , h , q , w , θ , and g denote the cross-sectional area, velocity, density, pressure, specific enthalpy, heat flow into the pipe per unit length and time, frictional force per unit length of pipe, angle of inclination, and gravitational acceleration, respectively. The symbols t and s correspond to the time and space variables, respectively. Furthermore, the spatiotemporal domain Ω can be described as $\Omega = \{(s, t) : 0 \leq s \leq L, 0 \leq t \leq t_f\}$, where t_f signifies the time span and L denotes the length of the pipeline. Utilizing the real gas equation of state $p = z\rho RT$ (where z , R , and T represent the gas compressibility factor, the ideal gas constant, and the temperature, respectively) and the thermodynamic identity [30], expressed as follows:

$$dh = C_p dT + \left(\frac{T}{\rho} \left(\frac{\partial \rho}{\partial T} \right)_p + 1 \right) \frac{dp}{\rho} \quad (4)$$

(where C_p denotes the specific heat at constant pressure), (1)–(3) can be restructured as the set of hyperbolic equations using temperature, velocity, and pressure as the dependent variables and are specified in [31]. The governing system of PDEs can be compactly represented in terms of pressure, mass flow rate, and temperature as follows:

$$\frac{\partial \mathbf{x}}{\partial t} + \mathbf{A}(\mathbf{x}) \frac{\partial \mathbf{x}}{\partial s} + \boldsymbol{\zeta}(\mathbf{x}) = 0 \quad (5)$$

where $\mathbf{x} = [p, \dot{m}, T]^T$ [32], [33]. When $\theta = \pi$, the coefficient matrix $\mathbf{A}(\mathbf{x}) \in \mathbb{R}^{3 \times 3}$ can be expressed as (6), shown at the bottom of the next page, and the vector $\boldsymbol{\zeta}(\mathbf{x}) \in \mathbb{R}^{3 \times 1}$ can be defined as shown in the equation at the bottom of the next page, where $\alpha_1 = 1 + (T/z)((\partial z/\partial T))_p$,

$\alpha_2 = 1 - (p/z)((\partial z/\partial p))_T$, and the isentropic wave speed is $a_s = (\partial p/\partial \rho)_s^{1/2}$ [29]. The frictional force per unit length is $w = (1/8)f\rho v|\pi d$, where the friction factor f is calculated using the Colebrook–White equation [34] and d is the diameter. Furthermore, the heat flow between the natural gas and its surroundings per unit length and time is defined as $q = -\pi dU(T - T_s)$, where U and T_s denote the overall heat transfer coefficient and ambient temperature, respectively. A steady-state heat transfer is assumed. The transport and thermodynamic properties, specifically z and C_p , are computed using GERG-2004 [35]. Moreover, validating the flow model for long-distance pipelines poses challenges. This difficulty arises from the fact that variables, such as internal pipe roughness, surrounding temperature, heat exchange, heat capacity, thermal conductivity, and diffusivity, undergo changes over time, and their accurate determination is challenging. Essentially, these quantities, which depend on spatial and time variables, are difficult to determine. The validation of the flow model in [36] showed that the discrepancies between modeled and measured flow values are most likely caused by physical approximation errors.

B. Numerical Method of Lines

The numerical method of lines, which relies on spatial discretization, serves as an effective approach for solving transient models involving the system of PDEs. This approach is a well-established generic method for solving time-dependent PDEs [37]. For spatial discretization, a five-point, fourth-order finite difference scheme is used, because it yields satisfactory results for the transient flow model containing mild fronts in the boundary conditions. The system of PDEs in (5) is spatially discretized to yield a set of ordinary differential equations (ODEs). This approximation exhibits an error of order $\mathcal{O}(\Delta s^4)$, where Δs represents the spatial step size. On spatial discretization, the system of ODEs can be given as follows:

$$\frac{d\mathbf{x}(t)}{dt} = \mathbf{A}(\mathbf{x})\mathbf{D}\mathbf{x}(t) - \boldsymbol{\zeta}(\mathbf{x}, t) \triangleq \boldsymbol{\varphi}(t, \mathbf{x}(t)) \quad (7)$$

where $\mathbf{A}(\mathbf{x}) \in \mathbb{R}^{3n \times 3n}$ denotes the assembled matrix, $\boldsymbol{\zeta}(\mathbf{x}, t) \in \mathbb{R}^{3n \times 1}$ represents the assembled column vector of $\boldsymbol{\zeta}(\mathbf{x})$, and the state vector \mathbf{x} becomes

$$\mathbf{x}(t) = [p_1(t), \dots, p_i(t), \dots, p_n(t), \dot{m}_1(t), \dots, \dot{m}_i(t), \dots, \dot{m}_n(t), T_1(t), \dots, T_i(t), \dots, T_n(t)]^T. \quad (8)$$

Furthermore, the computational matrix \mathbf{D} can be expressed as follows:

$$\mathbf{D} = -\frac{1}{12\Delta s} \begin{bmatrix} -25 & 48 & -36 & 16 & -3 & \dots & 0 \\ -3 & -10 & 18 & -6 & 1 & \dots & 0 \\ 1 & -8 & 0 & 8 & -1 & \dots & 0 \\ \vdots & \ddots & \ddots & \ddots & \ddots & \ddots & \vdots \\ 0 & \dots & 1 & -8 & 0 & 8 & -1 \\ 0 & \dots & -1 & 6 & -18 & 10 & 3 \\ 0 & \dots & 3 & -16 & 36 & -48 & 25 \end{bmatrix}.$$

The system of ODEs defined in (7) can be solved using the fourth-order Runge–Kutta method. The discretized equations with a constant time step can be formulated as a state-space model. Furthermore, its solution (advanced in time) is

$$\mathbf{x}(t + \Delta t) = \mathbf{x}(t) + \frac{1}{6}(\mathbf{k}_1 + 2\mathbf{k}_2 + 2\mathbf{k}_3 + \mathbf{k}_4)$$

where

$$\begin{aligned} \mathbf{k}_1 &= \Delta t \boldsymbol{\varphi}(t, \mathbf{x}(t)) \\ \mathbf{k}_2 &= \Delta t \boldsymbol{\varphi}\left(t + \frac{1}{2}\Delta t, \mathbf{x}(t) + \frac{1}{2}\mathbf{k}_1\right) \\ \mathbf{k}_3 &= \Delta t \boldsymbol{\varphi}\left(t + \frac{1}{2}\Delta t, \mathbf{x}(t) + \frac{1}{2}\mathbf{k}_2\right) \\ \mathbf{k}_4 &= \Delta t \boldsymbol{\varphi}(t + \Delta t, \mathbf{x}(t) + \mathbf{k}_3). \end{aligned}$$

To ensure numerical stability, it is crucial to satisfy the Courant–Friedrichs–Lewy condition [38], given as follows:

$$\frac{\Delta t}{\Delta s} \leq \frac{1}{|v| + a_s}. \quad (9)$$

Next, the proposed model-based SFDIA architecture for simultaneous multiple fault diagnosis is discussed.

III. MM-SFDIA ARCHITECTURE

The proposed architecture leverages the concept of state consistency within the framework of a distributed EnKF. More specifically, the architecture combines the benefits of several EnKFs for local state estimation while also possessing the capability to detect and isolate multiple potential faulty sensors. The incorporation of several local filters not only alleviates computational load, but also offers effective fault detection and isolation performance.

The schematic of the proposed MM-SFDIA architecture is shown in Fig. 1 and described as follows. Initially, all

$$\mathbf{A}(\mathbf{x}) = \begin{bmatrix} -\frac{\dot{m}(a_s^2\alpha_2 - RTz)}{Ap} & \frac{a_s^2}{A} & \frac{a_s^2\dot{m}\alpha_1}{AT} \\ A - \frac{a_s^2\alpha_2^2C_p\dot{m}^2 - Ra_s^2\alpha_1^2\alpha_2\dot{m}^2z}{ac_p p^2} & \frac{\dot{m}(\alpha_2C_p a_s^2 - Rz a_s^2\alpha_1^2 + RTC_p z)}{ac_p p} & \frac{a_s^2\alpha_1\dot{m}^2(\alpha_2C_p - Ra_s^2\alpha_1^2z)}{ATC_p p} \\ -\frac{RTa_s^2\alpha_1\alpha_2\dot{m}z}{ac_p p^2} & \frac{RTa_s^2\alpha_1z}{ac_p p} & \frac{R\dot{m}z(a_s^2\alpha_1^2 + TC_p)}{ac_p p} \end{bmatrix}$$

$$\boldsymbol{\zeta}(\mathbf{x}) = \begin{bmatrix} -\frac{a_s^2\alpha_1(Aqp + RT\dot{m}wz)}{A^2TC_p p} & w & -\frac{a_s^2\alpha_2(Aqp + RT\dot{m}wz)}{A^2C_p p^2} \end{bmatrix}^T \quad (6)$$

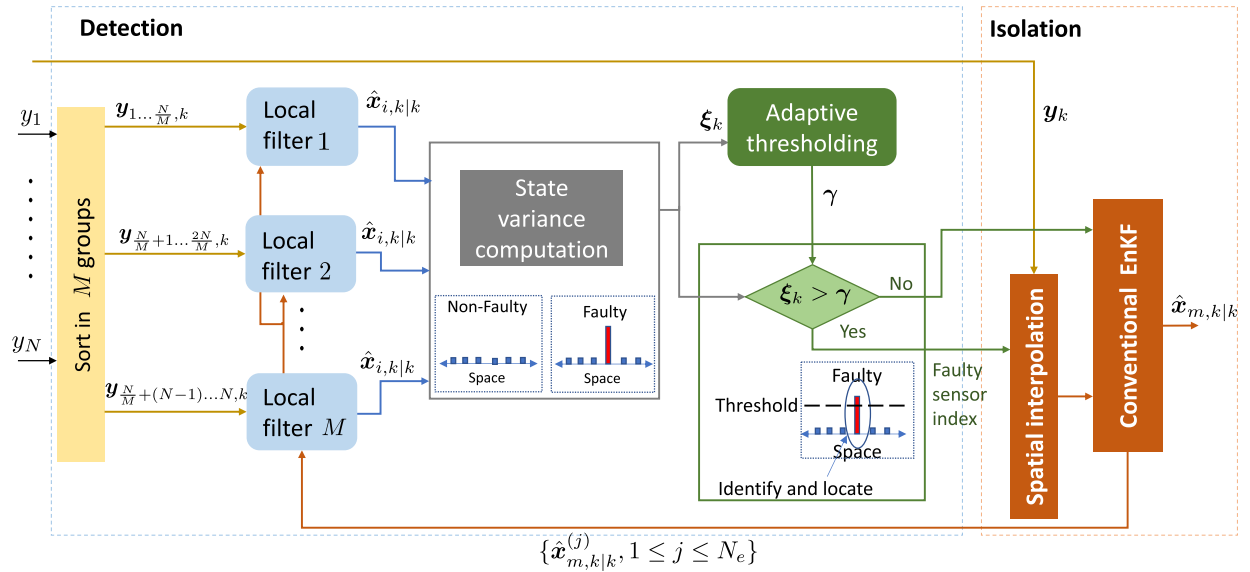


Fig. 1. Block diagram of the proposed MM-SFDIA architecture.

sensor measurements are partitioned into various subsets. Subsequently, the local EnKFs operate simultaneously to estimate the local state vectors and their associated covariances using their specific subset of measurements. The sensor faults are diagnosed by comparing the state variance vector against an adaptable threshold, which is dynamically calibrated using the state variance vectors. Upon identifying a faulty sensor, the corresponding corrected measurement is determined via interpolation across the spatial domain (relying on measurements from nonfaulty sensors). Using the corrected sensor measurements, the global estimates are generated utilizing the conventional EnKF, which are fed back to the locals for initialization during the subsequent iteration. All the steps required to implement the MM-SFDIA architecture are comprehensively discussed in the following subsections.

A. Grouping of Sensors

The initial step in the distributed filtering-based approach involves the grouping of sensor measurements. A unique grouping strategy, where each local filter is assigned a distinct set of measurements, is utilized. The number of locals, denoted by M , is chosen based on a specific use case. The N sensor measurements are divided among the M locals in such a way that each local filter is assigned a distinct set of N/M measurements.¹ Subsequently, each local filter yields its independent state estimate based on its own set of measurements. By employing the state consistency strategy, which ensures that the estimated local state vectors from different local filters exhibit consistency in the absence of sensor faults, it becomes possible to analyze the variations among these independent local state vector estimates. This approach proves to be highly effective in detecting faulty sensors, thus rendering the proposed architecture a robust and reliable solution for fault detection. However, it is crucial to highlight that the state consistency approach can be effectively

¹For sake of simplicity, we assume that N/M is an integer number.

applied only when the sensor measurements are independent and uncorrelated. In the following subsection, the design of the local filter employed within the distributed framework is investigated.

B. Local Filter Design

The nonlinear discrete-time process model at the k th discrete time for the i th local filter ($i = 1, 2, \dots, M$) can be described as follows:

$$\mathbf{x}_{i,k} = \mathbf{f}_i(\mathbf{x}_{i,k-1}, \mathbf{u}_{k-1}) + \mathbf{v}_{i,k} \quad (10)$$

where $\mathbf{v}_{i,k} \in \mathbb{R}^{n_x \times 1} \sim \mathcal{N}(\mathbf{0}, \mathbf{Q}_{i,k})$ is the process noise and the nonlinear mapping $\mathbf{f}_i(\cdot) : \mathbb{R}^{n_x} \times \mathbb{R}^{n_u} \rightarrow \mathbb{R}^{n_x}$ represents the process model for the i th local filter. The input vector $\mathbf{u}_{k-1} \in \mathbb{R}^{n_u \times 1}$ comprising of the initial and boundary conditions is defined as $\mathbf{u}_{k-1} = [\mathbf{u}_{\text{in}}^T \mathbf{u}_{\text{bc},k-1}^T]^T$. The local-filter state vector $\mathbf{x}_{i,k} \in \mathbb{R}^{n_x \times 1}$ is

$$\mathbf{x}_{i,k} = [p_1(k), \dots, p_n(k), \dot{m}_1(k), \dots, \dot{m}_n(k), T_1(k), \dots, T_n(k)]^T. \quad (11)$$

The measurement model at the k th discrete time for the i th local filter can be expressed as follows:

$$\mathbf{y}_{i,k} = \mathbf{h}_i(\mathbf{x}_{i,k}, \mathbf{u}_k) + \mathbf{n}_{i,k} \quad (12)$$

where $\mathbf{n}_{i,k} \in \mathbb{R}^{n_y \times 1} \sim \mathcal{N}(\mathbf{0}, \mathbf{R}_{i,k})$ is the measurement noise, $\mathbf{y}_{i,k} \in \mathbb{R}^{n_y \times 1}$ corresponds to the filter output, and the mapping $\mathbf{h}_i(\cdot, \cdot) : \mathbb{R}^{n_x} \times \mathbb{R}^{n_u} \rightarrow \mathbb{R}^{n_y}$ represents the measurement model. For our specific case, a linear model is considered, and the mapping \mathbf{h}_i for the i th local filter is chosen as follows:

$$\mathbf{h}_i(\mathbf{x}_{i,k}, \mathbf{u}_k) = \mathbf{H}_i \mathbf{x}_{i,k} \quad (13)$$

where $\mathbf{H}_i \in \mathbb{R}^{n_y \times n_x}$ represents the observation matrix for the i th local filter [39]. The aim is to facilitate one-to-one mapping for dimensionality reduction of the state vector according to the number of measurements assigned to the i th local filter.

For the proposed distributed framework, EnKFs are utilized as local filters. This selection offers numerous benefits over other variants of the KF concerning the stability and scalability of our framework. The EnKF demonstrates exceptional efficacy in handling high-dimensional nonlinear systems. Moreover, it exhibits enhanced stability and faster convergence rates, even when the local filters lack full observability (i.e., all observations are not available to each local filter). The expected performance of our proposed SFDIA architecture remains largely unaffected, even when applied to an extended transmission line setup.

The various steps involved in the state estimation process of the local EnKF are discussed below.

Initialization: The local state vector estimate $\hat{\mathbf{x}}_{i,0|0}$ and local covariance matrix $\mathbf{P}_{i,0|0}$ are initialized for each local filter depending on the use case.

Ensemble of Samples Computation: An ensemble of samples, $\{\hat{\mathbf{x}}_{i,k-1|k-1}^{(j)}, j = 1, 2, \dots, N_e\}$, approximately representing $p(\mathbf{x}_{i,k-1}|\mathbb{Y}_{i,k-1})$, where N_e is the ensemble size and $\mathbb{Y}_{i,k-1} = \{\mathbf{y}_{i,1}, \mathbf{y}_{i,2}, \dots, \mathbf{y}_{i,k-1}\}$, is generated. Also, an ensemble of noise samples, $\{\mathbf{v}_{i,k}^{(j)}, j = 1, 2, \dots, N_e\}$, is drawn to represent the process noise distribution $\mathcal{N}(\mathbf{0}, \mathbf{Q}_{i,k})$. The initially generated ensemble of the state estimate for the i th local filter, namely, $\mathcal{X}_{i,0|0} \in \mathbb{R}^{n_x \times N_e}$, includes samples in the form

$$\hat{\mathbf{x}}_{i,0|0}^{(j)} = \hat{\mathbf{x}}_{i,0|0} + \mathbf{v}_{i,0}^{(j)}, \quad j = 1, 2, \dots, N_e. \quad (14)$$

Time and Measurement Updates: In the time update step, the a priori ensemble $\{\hat{\mathbf{x}}_{i,k|k-1}^{(j)}, j = 1, 2, \dots, N_e\}$ representing $p(\mathbf{x}_{i,k}|\mathbb{Y}_{i,k-1})$ for the i th local filter can be given as follows:

$$\hat{\mathbf{x}}_{i,k|k-1}^{(j)} = \mathbf{f}_i\left(\hat{\mathbf{x}}_{i,k-1|k-1}^{(j)}, \mathbf{u}_{k-1}^{(j)}\right) + \mathbf{v}_{i,k}^{(j)}. \quad (15)$$

The sample mean and covariance of the a priori ensemble can be calculated as follows:

$$\begin{aligned} \hat{\mathbf{x}}_{i,k|k-1} &= \frac{1}{N_e} \sum_{j=1}^{N_e} \hat{\mathbf{x}}_{i,k|k-1}^{(j)} \\ \mathbf{P}_{i,k|k-1} &= \frac{1}{N_e - 1} \mathbf{E}_{i,k|k-1}^x (\mathbf{E}_{i,k|k-1}^x)^T \end{aligned} \quad (16)$$

where the matrix $\mathbf{E}_{i,k|k-1}^x$ is defined as $\mathbf{E}_{i,k|k-1}^x = [(\hat{\mathbf{x}}_{i,k|k-1}^{(1)} - \hat{\mathbf{x}}_{i,k|k-1}), \dots, (\hat{\mathbf{x}}_{i,k|k-1}^{(N_e)} - \hat{\mathbf{x}}_{i,k|k-1})]$. Next, an ensemble of samples $\{\hat{\mathbf{y}}_{i,k|k-1}^{(j)}, j = 1, 2, \dots, N_e\}$ is constructed to represent $p(\mathbf{y}_{i,k}|\mathbb{Y}_{i,k-1})$, which can be given as follows:

$$\hat{\mathbf{y}}_{i,k|k-1}^{(j)} = \mathbf{h}_i\left(\hat{\mathbf{x}}_{i,k|k-1}^{(j)}, \mathbf{u}_k^{(j)}\right) + \mathbf{n}_{i,k}^{(j)} \quad (17)$$

where the ensemble of samples $\{\mathbf{n}_{i,k}^{(j)}, j = 1, 2, \dots, N_e\}$ is produced as per the Gaussian distribution $\mathcal{N}(\mathbf{0}, \mathbf{R}_{i,k})$ to define the measurement noise. The sample mean and covariance of this ensemble are

$$\begin{aligned} \hat{\mathbf{y}}_{i,k|k-1} &= \frac{1}{N_e} \sum_{j=1}^{N_e} \hat{\mathbf{y}}_{i,k|k-1}^{(j)} \\ \mathbf{P}_{i,k|k-1}^y &= \frac{1}{N_e - 1} \mathbf{E}_{i,k|k-1}^y (\mathbf{E}_{i,k|k-1}^y)^T \end{aligned} \quad (18)$$

where the matrix $\mathbf{E}_{i,k|k-1}^y = [(\hat{\mathbf{y}}_{i,k|k-1}^{(1)} - \hat{\mathbf{y}}_{i,k|k-1}), \dots, (\hat{\mathbf{y}}_{i,k|k-1}^{(N_e)} - \hat{\mathbf{y}}_{i,k|k-1})]$. The cross covariance between $\mathbf{x}_{i,k}$ and $\mathbf{y}_{i,k}$ given $\mathbb{Y}_{i,k-1}$ is

$$\mathbf{P}_{i,k|k-1}^{xy} = \frac{1}{N_e - 1} \mathbf{E}_{i,k|k-1}^x (\mathbf{E}_{i,k|k-1}^y)^T.$$

Next, each member $\{\hat{\mathbf{x}}_{i,k|k-1}^{(j)}\}$ of the a priori ensemble is updated based on the latest measurement $\mathbf{y}_{i,k}$ as follows:

$$\hat{\mathbf{x}}_{i,k|k}^{(j)} = \hat{\mathbf{x}}_{i,k|k-1}^{(j)} + \mathbf{K}_{i,k} (\mathbf{y}_{i,k} - \hat{\mathbf{y}}_{i,k|k-1}^{(j)}) \quad (19)$$

$$\mathbf{K}_{i,k} = \mathbf{P}_{i,k|k-1}^{xy} (\mathbf{P}_{i,k|k-1}^y)^{-1}. \quad (20)$$

The a posteriori ensemble $\{\hat{\mathbf{x}}_{i,k|k}^{(j)}, j = 1, 2, \dots, N_e\}$ provides an approximate representation of the conditional probability distribution $p(\mathbf{x}_{i,k}|\mathbb{Y}_{i,k})$ for the i th local filter at the k th time instant. The updated estimate of the mean and covariance can be determined using the a posteriori ensemble as follows:

$$\begin{aligned} \hat{\mathbf{x}}_{i,k|k} &= \frac{1}{N_e} \sum_{j=1}^{N_e} \hat{\mathbf{x}}_{i,k|k}^{(j)} \\ \mathbf{P}_{i,k|k} &= \frac{1}{N_e - 1} \mathbf{E}_{i,k|k}^x (\mathbf{E}_{i,k|k}^x)^T \end{aligned} \quad (21)$$

where the matrix $\mathbf{E}_{i,k|k}^x$ is defined as $\mathbf{E}_{i,k|k}^x = [(\hat{\mathbf{x}}_{i,k|k}^{(1)} - \hat{\mathbf{x}}_{i,k|k}), \dots, (\hat{\mathbf{x}}_{i,k|k}^{(N_e)} - \hat{\mathbf{x}}_{i,k|k})]$. The above ensemble-based prediction and update are iteratively applied in a recursive manner. The various steps involved in the implementation of the i th local EnKF filter are summarized in Algorithm 1. Moreover, the EnKF's time and measurement updates are explicitly outlined as follows.

Time Update:

$$\hat{\mathbf{x}}_{i,k|k-1}^{(j)} = \mathbf{f}_i\left(\hat{\mathbf{x}}_{i,k-1|k-1}^{(j)}, \mathbf{u}_{k-1}^{(j)}\right) + \mathbf{v}_{i,k}^{(j)}$$

$$\hat{\mathbf{y}}_{i,k|k-1}^{(j)} = \mathbf{h}_i\left(\hat{\mathbf{x}}_{i,k|k-1}^{(j)}, \mathbf{u}_k^{(j)}\right) + \mathbf{n}_{i,k}^{(j)}$$

$$\hat{\mathbf{x}}_{i,k|k-1} = \frac{1}{N_e} \sum_{j=1}^{N_e} \hat{\mathbf{x}}_{i,k|k-1}^{(j)}$$

$$\hat{\mathbf{y}}_{i,k|k-1} = \frac{1}{N_e} \sum_{j=1}^{N_e} \hat{\mathbf{y}}_{i,k|k-1}^{(j)}$$

$$\mathbf{E}_{i,k|k-1}^x = [(\hat{\mathbf{x}}_{i,k|k-1}^{(1)} - \hat{\mathbf{x}}_{i,k|k-1}), \dots, (\hat{\mathbf{x}}_{i,k|k-1}^{(N_e)} - \hat{\mathbf{x}}_{i,k|k-1})]$$

$$\mathbf{E}_{i,k|k-1}^y = [(\hat{\mathbf{y}}_{i,k|k-1}^{(1)} - \hat{\mathbf{y}}_{i,k|k-1}), \dots, (\hat{\mathbf{y}}_{i,k|k-1}^{(N_e)} - \hat{\mathbf{y}}_{i,k|k-1})]$$

$$\mathbf{P}_{i,k|k-1} = \frac{1}{N_e - 1} \mathbf{E}_{i,k|k-1}^x (\mathbf{E}_{i,k|k-1}^x)^T.$$

Measurement Update:

$$\mathbf{P}_{i,k|k-1}^{xy} = \frac{1}{N_e - 1} \mathbf{E}_{i,k|k-1}^x (\mathbf{E}_{i,k|k-1}^y)^T$$

$$\mathbf{P}_{i,k|k-1}^y = \frac{1}{N_e - 1} \mathbf{E}_{i,k|k-1}^y (\mathbf{E}_{i,k|k-1}^y)^T$$

$$\mathbf{K}_{i,k} = \mathbf{P}_{i,k|k-1}^{xy} (\mathbf{P}_{i,k|k-1}^y)^{-1}$$

$$\hat{\mathbf{x}}_{i,k|k}^{(j)} = \hat{\mathbf{x}}_{i,k|k-1}^{(j)} + \mathbf{K}_{i,k} (\mathbf{y}_{i,k} - \hat{\mathbf{y}}_{i,k|k-1}^{(j)})$$

Algorithm 1 Implementation of the i th Local EnKF Filter During the k th Time Instant

Input: Ensemble of samples at the $(k - 1)$ th time instant $\{\hat{\mathbf{x}}_{i,k-1|k-1}^{(j)}, 1 \leq j \leq N_e\}$

1 **Step 1: Generate a priori ensemble:**

2 **for** each sample **do**

3 Process model update using eq. (15)

4 **end for**

5 A priori state estimate and covariance using eq. (16)

6 **Step 2: Generate measurement ensemble:**

7 **for** each sample **do**

8 Measurement model update using eq. (17)

9 **end for**

10 Sample mean and covariance of the measurement ensemble using eq. (18)

11 **Step 3: Generate a posteriori measurement ensemble:**

12 **for** each sample **do**

13 Update each a priori sample by incorporating the k th measurement using eq. (19) and eq. (20)

14 **end for**

15 **Step 4: Compute local state estimate and covariance:**

16 Obtain sample mean and covariance of the a posteriori ensemble using eq. (21)

Output: Local state estimate $\hat{\mathbf{x}}_{i,k|k}$, and covariance $\hat{\mathbf{P}}_{i,k|k}$ at the k th time instant

$$\begin{aligned}\hat{\mathbf{x}}_{i,k|k} &= \frac{1}{N_e} \sum_{j=1}^{N_e} \hat{\mathbf{x}}_{i,k|k}^{(j)} \\ \mathbf{E}_{i,k|k}^x &= \left[\left(\hat{\mathbf{x}}_{i,k|k}^{(1)} - \hat{\mathbf{x}}_{i,k|k} \right), \dots, \left(\hat{\mathbf{x}}_{i,k|k}^{(N_e)} - \hat{\mathbf{x}}_{i,k|k} \right) \right] \\ \mathbf{P}_{i,k|k} &= \frac{1}{N_e - 1} \mathbf{E}_{i,k|k}^x \left(\mathbf{E}_{i,k|k}^x \right)^T.\end{aligned}$$

Employing the grouping technique discussed in Section III-A, the i th local filter generates the local state vector estimate $\hat{\mathbf{x}}_{i,k|k}$ using the measurement subset $\mathbf{y}_{i,k}$, where $\hat{\mathbf{x}}_{i,k|k}$ represents the complete measurement vector $\mathbf{y}_{i,k}$. It is worth noting that the local measurement group $\mathbf{y}_{i,k}$ only influences the corresponding elements in the local state estimate $\hat{\mathbf{x}}_{i,k|k}$. Moreover, the Kalman gain matrix $\mathbf{K}_{i,k}$ plays a critical role during the measurement update of the local filter, as it significantly impacts the a posteriori state estimate. The assumption that all measurements are independent and uncorrelated enables us to selectively set only those columns of the $\mathbf{K}_{i,k}$ to nonzero values, which correspond to the measurements present in both $\hat{\mathbf{x}}_{i,k|k}$ and $\mathbf{y}_{i,k}$ while setting the rest of the entries to zero. For instance, if the c th measurement is missing from the subset $\mathbf{y}_{i,k}$, then all the elements in the c th column of the gain matrix $\mathbf{K}_{i,k}$ are set to zero. Consequently, the a posteriori estimates of the remaining subsets remain equal to the a priori estimates. Hence, this approach ensures that the local measurement subset solely affects its respective elements in the state vector estimate, leaving the other elements unchanged. In the following

subsection, we will discuss how this grouping technique facilitates fault detection.

C. Fault Detection

For fault detection, the state-variance vector ($\xi_k \in \mathbb{R}^{n_x \times 1}$) serves as an anomaly indicator. Its ℓ th entry $\xi_{\ell,k}$ is defined as follows:

$$\xi_{\ell,k} = \sqrt{\frac{1}{M} \sum_{i=1}^M \left(\hat{x}_{i,k|k}^{(\ell)} - \frac{1}{M} \sum_{i=1}^M \hat{x}_{i,k|k}^{(\ell)} \right)^2} \quad (22)$$

where $\hat{x}_{i,k|k}^{(\ell)}$ represents the ℓ th entry of the i th local-filter state estimate $\hat{\mathbf{x}}_{i,k|k}$. When a fault occurs, the entries of the state-variance vector will increase, thus facilitating fault detection. Specifically, when the parameter $\xi_{\ell,k}$ exceeds a predetermined threshold γ_ℓ , we infer the presence of a fault, i.e.,

$$d_{\ell,k} = \begin{cases} 1, & \xi_{\ell,k} > \gamma_\ell \\ 0, & \xi_{\ell,k} < \gamma_\ell. \end{cases} \quad (23)$$

Once a faulty condition is identified, it is crucial to determine the exact location of the faulty sensors. This task can be accomplished by analyzing the components of the state-variance vector ξ_k that meet the aforementioned criterion. It is important to highlight that this approach can be utilized to identify multiple sensor faults occurring simultaneously. To elaborate, when the state-variance values $\xi_{\ell,k}$, $\xi_{p,k}$, and $\xi_{n,k}$ exceed the threshold γ_ℓ , it indicates a fault in the sensors corresponding to positions ℓ , p , and n . Furthermore, the set containing the location of the faulty sensors can be defined as follows:

$$\mathcal{F} = \{l : \xi_{l,k} > \gamma_\ell\}. \quad (24)$$

While traditional fault detection can be accomplished using the fixed thresholding technique. However, conventional fixed thresholds may encounter difficulties in adapting to varying environmental conditions, leading to false positives or missed detections. Hence, enhancing the accuracy and responsiveness of the fault detection system highlights the necessity of leveraging adaptive thresholding for fault diagnosis. This topic is comprehensively explored in the subsequent subsection.

D. Adaptive Thresholding

Given the inherent uncertainties in real systems, designing appropriate thresholds for accurately determining the location of the faulty sensors becomes a crucial aspect of fault diagnosis. While evaluating appropriate threshold values, opting for smaller thresholds enhances the probability of encountering false alarms, whereas favoring larger thresholds contributes to more missed alarms and reduced fault detection sensitivity. Hence, adopting an adaptive thresholding approach becomes essential to facilitate robust sensor fault detection against uncertainties, while also mitigating the occurrence of false alarms [40], [41].

To implement the time-varying adaptive thresholding mechanism, an error metric $\mathbf{E}_k \triangleq [\mathbf{e}_{1,k}, \mathbf{e}_{2,k}, \mathbf{e}_{3,k}, \dots, \mathbf{e}_{N,k}] \in \mathbb{R}^{m \times N}$ is considered, where N signifies the number of sensors. To evaluate the ℓ th sensor error metric $e_{\ell,k} \in \mathbb{R}^{m \times 1}$, a moving

window of fixed length m is employed. The generation of $e_{\ell,k}$ utilizes state-variance values corresponding to the current and previous time instances that satisfy the condition $\xi_{\ell,k} < \gamma_{\ell}$. Hence, the error metric $e_{\ell,k}$ can be formulated as follows:

$$e_{\ell,k} = [\xi_{\ell,k-m}, \xi_{\ell,k-m+1}, \dots, \xi_{\ell,k-1}, \xi_{\ell,k}]^T. \quad (25)$$

The mean $\mu_{e,\ell,k}$ and variance $\sigma_{e,\ell,k}$ of the error metric $e_{\ell,k}$ can be evaluated as follows:

$$\begin{aligned} \mu_{e,\ell,k} &= \frac{1}{m} \sum_{j=k-m}^k \xi_{\ell,j} \\ \sigma_{e,\ell,k} &= \frac{1}{m} \sum_{j=k-m}^k \left(\xi_{\ell,j} - \frac{1}{m} \sum_{j=k-m}^k (\xi_{\ell,j}) \right)^2 \end{aligned} \quad (26)$$

where $\xi_{\ell,j}$ is the ℓ th entry of the state-variance vector ξ_j at the j th time instant. Using the abovementioned statistics, the ℓ th entry of the adaptive threshold vector γ_k during the k th time instant, defined by $\gamma_{\ell,k}$, can be computed as follows:

$$\gamma_{\ell,k} = r\mu_{e,\ell,k} + \lambda\sigma_{e,\ell,k} \quad (27)$$

where the tuning factors r , λ , and the time-window m are chosen based on the specific use case and the desired performance goals. Note that under normal conditions without faults, m remains fixed. However, in the presence of a fault, m becomes variable. For instance, when a fault occurs at the k th time instant, the error metric $e_{\ell,k}$ stops updating the state-variance values associated with the current ($\xi_{\ell,k}$) and subsequent time instances. Consequently, the number of state-variance values included in $e_{\ell,k}$ decreases. Nevertheless, it is essential to ensure that m does not fall below its threshold value m_t , thereby satisfying the condition $m \not< m_t$.

Conversely, the adaptive threshold gradually achieves a smoother and more accurate value with the increasing value of m . However, a larger value of m cannot be employed due to computational constraints. By appropriately adjusting the tuning factors, a desired level of the threshold can be determined. This demonstrates the robustness of the adaptive thresholding method in fault detection, particularly in spatiotemporal systems where nonfaulty neighboring sensors may also exhibit high state-variance values. The adaptive threshold dynamically modifies its threshold value based on the observed state-variance values from both faulty and nonfaulty sensors. Consequently, the adaptive thresholding approach significantly enhances the accurate detection of faulty sensor positions, facilitating the effective isolation and handling of erroneous sensor measurements.

E. Isolation and Accommodation

After identification of the faulty sensor locations using the techniques discussed in Sections III-C and III-D, it becomes feasible to readily isolate the faulty sensors and replace their flawed measurements with measurements obtained through interpolation across the spatial domain. Given that the proposed framework is based on the distributed system with spatiotemporal dynamics, the exact locations of the nonfaulty sensors across the space are known. For instance, if the sensor

at the ℓ th spatial location is faulty, the accurate measurement for the ℓ th sensor can be determined through 1-D linear interpolation, utilizing measurements of the neighboring nonfaulty sensors. Similarly, when an array of sensors is identified as faulty, one can leverage the nonfaulty sensors located at the boundary for interpolation. In the final stage, the corrected measurements are used to compute the final fault-free state vector estimate $\hat{\mathbf{x}}_{m,k|k}$ using a conventional EnKF. The various steps involved in the implementation of conventional EnKF are summarized below.

Initialization: The state vector estimate $\hat{\mathbf{x}}_{0|0}$ and covariance matrix $\mathbf{P}_{0|0}$ for the conventional filter are initialized.

Initial Ensemble Point Computation: The initial ensemble of state estimates $\{\hat{\mathbf{x}}_{0|0}^{(j)}, j = 1, 2, \dots, N_e\}$ is generated using an ensemble of samples $\{\mathbf{v}_0^{(j)}, j = 1, 2, \dots, N_e\}$ drawn from the Gaussian distribution $\mathcal{N}(\mathbf{0}, \mathbf{Q}_k)$.

Time and Measurement Update: At each update step, a new set of samples $\{\hat{\mathbf{x}}_{k|k-1}^{(j)}, j = 1, 2, \dots, N_e\}$ is generated using an ensemble of samples $\{\mathbf{v}_k^{(j)}, j = 1, 2, \dots, N_e\}$ drawn from the Gaussian distribution $\mathcal{N}(\mathbf{0}, \mathbf{Q}_k)$.

Time Update:

$$\begin{aligned} \hat{\mathbf{x}}_{k|k-1}^{(j)} &= \mathbf{f}(\hat{\mathbf{x}}_{k-1|k-1}^{(j)}, \mathbf{u}_{k-1}^{(j)}) + \mathbf{v}_k^{(j)} \\ \hat{\mathbf{y}}_{k|k-1}^{(j)} &= \mathbf{h}(\hat{\mathbf{x}}_{k|k-1}^{(j)}, \mathbf{u}_k^{(j)}) + \mathbf{n}_k^{(j)} \\ \hat{\mathbf{x}}_{k|k-1} &= \frac{1}{N_e} \sum_{j=1}^{N_e} \hat{\mathbf{x}}_{k|k-1}^{(j)} \\ \hat{\mathbf{y}}_{k|k-1} &= \frac{1}{N_e} \sum_{j=1}^{N_e} \hat{\mathbf{y}}_{k|k-1}^{(j)} \\ \mathbf{E}_{k|k-1}^x &= \left[(\hat{\mathbf{x}}_{k|k-1}^{(1)} - \hat{\mathbf{x}}_{k|k-1}), \dots, (\hat{\mathbf{x}}_{k|k-1}^{(N_e)} - \hat{\mathbf{x}}_{k|k-1}) \right] \\ \mathbf{E}_{k|k-1}^y &= \left[(\hat{\mathbf{y}}_{k|k-1}^{(1)} - \hat{\mathbf{y}}_{k|k-1}), \dots, (\hat{\mathbf{y}}_{k|k-1}^{(N_e)} - \hat{\mathbf{y}}_{k|k-1}) \right] \\ \mathbf{P}_{k|k-1} &= \frac{1}{N_e - 1} \mathbf{E}_{k|k-1}^x (\mathbf{E}_{k|k-1}^x)^T. \end{aligned}$$

Measurement Update:

$$\begin{aligned} \mathbf{P}_{k|k-1}^{xy} &= \frac{1}{N_e - 1} \mathbf{E}_{k|k-1}^x (\mathbf{E}_{k|k-1}^y)^T \\ \mathbf{P}_{k|k-1}^y &= \frac{1}{N_e - 1} \mathbf{E}_{k|k-1}^y (\mathbf{E}_{k|k-1}^y)^T \\ \mathbf{K}_k &= \mathbf{P}_{k|k-1}^{xy} (\mathbf{P}_{k|k-1}^y)^{-1} \\ \hat{\mathbf{x}}_{m,k|k}^{(j)} &= \hat{\mathbf{x}}_{k|k-1}^{(j)} + \mathbf{K}_k (\mathbf{y}_k - \hat{\mathbf{y}}_{k|k-1}^{(j)}) \\ \hat{\mathbf{x}}_{m,k|k} &= \frac{1}{N_e} \sum_{j=1}^{N_e} \hat{\mathbf{x}}_{m,k|k}^{(j)} \\ \mathbf{E}_{k|k}^x &= \left[(\hat{\mathbf{x}}_{m,k|k}^{(1)} - \hat{\mathbf{x}}_{m,k|k}), \dots, (\hat{\mathbf{x}}_{m,k|k}^{(N_e)} - \hat{\mathbf{x}}_{m,k|k}) \right] \\ \mathbf{P}_{m,k|k} &= \frac{1}{N_e - 1} \mathbf{E}_{k|k}^x (\mathbf{E}_{k|k}^x)^T. \end{aligned}$$

The ensemble of samples $\{\hat{\mathbf{x}}_{m,k|k}^{(j)}, j = 1, 2, \dots, N_e\}$ is subsequently shared with the local filters and is used as a prior information during the next iteration. Furthermore, the

Algorithm 2 MM-SFDIA Architecture in the Presence of Multiple Sensor Faults

Input: Number of locals M , boundary condition \mathbf{u}_{bc} and ensemble size N_e

- 1 **Initialization:** $\hat{\mathbf{x}}_{i,0|0} = \hat{\mathbf{x}}_{0|0}$, $\mathbf{P}_{i,0|0} = \mathbf{P}_{0|0}$
- 2 Initialize ensembles of local EnKFs $\{\hat{\mathbf{x}}_{i,0|0}^{(j)}\}$ and conventional EnKF $\{\hat{\mathbf{x}}_{0|0}^{(j)}\}$
- 3 **while** $k < k_{end}$ **do**
- 4 **Local filters:** Compute local estimates $\hat{\mathbf{x}}_{i,k|k}$ and $\mathbf{P}_{i,k|k}$ using time and measurement updates
- 5 **Fault detection:**
- 6 Compute state-variance vector ξ_k using eq. (22) and adaptive threshold γ_k using eq. (27)
- 7 **for** $\ell = 1, 2, \dots, N$ **do**
- 8 **if** $\xi_{\ell,k} > \gamma_{\ell,k}$ **then**
- 9 Fault in ℓ th sensor
- 10 ℓ th sensor measurement correction using spatial interpolation
- 11 **else**
- 12 No fault
- 13 **end if**
- 14 **end for**
- 15 **Conventional filter:** Compute global estimates $\hat{\mathbf{x}}_{m,k|k}$ and $\mathbf{P}_{m,k|k}$ using fault-free measurements
- 16 **Assign global ensemble to locals:** $\hat{\mathbf{x}}_{i,k|k}^{(j)} = \hat{\mathbf{x}}_{m,k|k}^{(j)}$
- 17 $k \leftarrow k + 1$
- 18 **end while**

Output: Fault-free global estimates $\hat{\mathbf{x}}_m$ and \mathbf{P}_m

TABLE II
PARAMETERS UTILIZED FOR SIMULATIONS

Parameters	Values
L	150 km
d	1.4 m
ϵ	0.016 mm
T_s	5°C
U	2.84 Wm ⁻² K ⁻¹

various steps involved to implement the proposed MM-SFDIA architecture are outlined in Algorithm 2.

IV. NUMERICAL RESULTS

To demonstrate the efficacy of our proposed architecture, we generate simulated data by employing a numerical solution of the transient flow model for the natural gas described in Section II. We opted for a high-pressure natural-gas pipeline employing the parameters outlined in Table II. The simulations are conducted over a time span of $t_f \in [0, 3600]$ s, with the initial conditions of $p(0, t) = 8.4$ MPa, $T(0, t) = 303.15$ K, and $\dot{m}(L, t) = f(t)$. The boundary conditions align with those in [29]. For the numerical solution of the transient-flow model, we consider the spatial and temporal step sizes as $\Delta s = 7500$ m and $\Delta t = 10$ s, respectively. Fig. 2 illustrates the boundary conditions and the associated spatial-temporal evolution of the state variables in the absence of additive noise. Moreover, Fig. 2(a) depicts the boundary conditions for flow

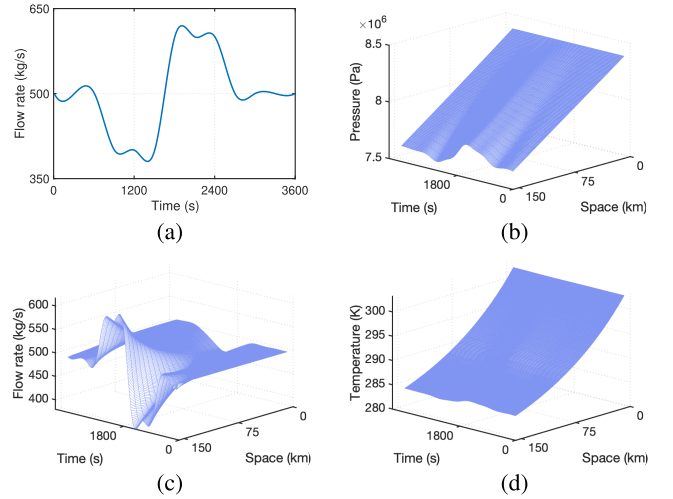


Fig. 2. Simulated data. (a) Boundary conditions. (b) Pressure. (c) Flow rate. (d) Temperature.

rate, highlighting rapid changes in the solution domain. These changes may potentially stem from disturbances in gas demand or changes in the operating conditions of system-controlling devices, such as valves, compressors, and pressure regulators.

To generate the noisy fault-free measurement for the j th sensor at the k th time instant ($y_j[k]$), we superimpose zero-mean white Gaussian noise ($q_j[k]$) to the generated ideal (devoid of both noise and fault) value ($x_j[k]$)

$$y_j[k] = x_j[k] + q_j[k]. \quad (28)$$

The measurement noises ($q_j[k]$) are generated according to the distributions $\mathcal{N}(0, 0.0005^2)$, $\mathcal{N}(0, 1.5^2)$, and $\mathcal{N}(0, 2.5^2)$ with variance in MPa², K², and (kg/s)² corresponding to pressure, temperature, and flow rate, respectively.

To assess the performance of the proposed MM-SFDIA framework, the synthetically generated fault signals are added to the simulated data obtained from the transient-flow model. This process emulates sensor measurements in the presence of sensor faults. Moreover, sensors can experience different types of faults, including bias, drift, freezing, and random faults, which are among the most commonly observed [3], [4]. While maintaining generality, we focused on bias and drift faults to exemplify hard and soft failures, respectively. The mathematical models for these fault types are as follows.

- 1) *Bias Fault:* A consistent level (or bias) b is introduced to the sensor measurements for a duration of G consecutive samples, denoted as follows:

$$y_j^f[k] = \begin{cases} y_j[k] + b, & 0 \leq k - g \leq G \\ y_j[k], & \text{else} \end{cases}$$

where $y_j^f[k]$ denotes the faulty measurement, while g signifies the onset time of the fault.

- 2) *Drift Fault:* The actual measurement gradually shifts upward (up to a maximum bias level b) over the span

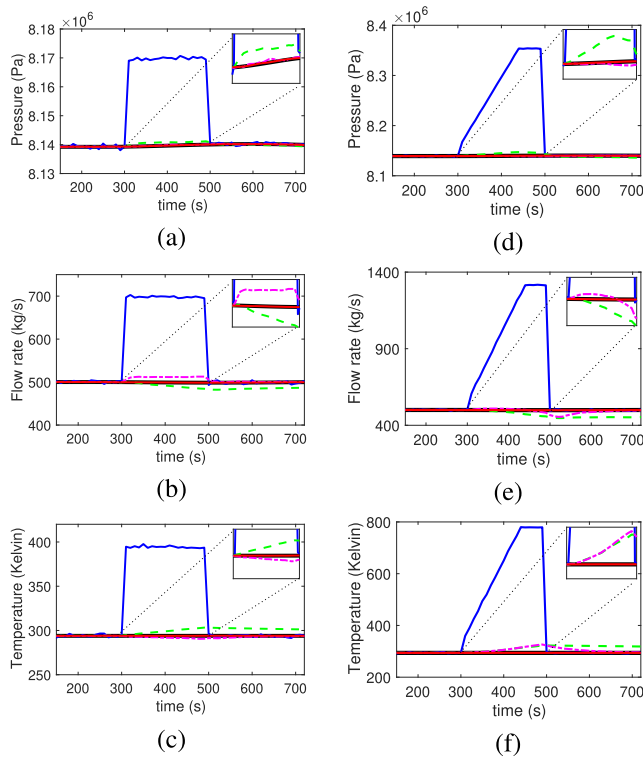


Fig. 3. State estimation using classic EnKF (green), fusing UKF (purple) [18], and proposed MM-SFDIA (red) techniques in the presence of three simultaneous bias and drift faults at indices $\ell = 8, 29$, and 50 . (a)–(c) [resp. (d)–(f)] Results for bias (resp. drift) faults, where actual and faulty values are depicted in black and blue, respectively.

of G time instances, i.e.,

$$y_j^f[k] = \begin{cases} y_j[k] + \frac{b(k-g+1)}{G}, & 0 \leq k-g \leq G \\ y_j[k] + b, & G \leq k-g \leq G+K \\ y_j[k], & \text{else.} \end{cases}$$

Here, K signifies the count of samples over which the drift fault sustains the saturated bias level b . Moreover, we emphasized the influence of the drift by assuming $G > K$.

The efficacy of the proposed strategies is explored in the presence of various sensor fault types. In particular, we investigate weak and strong faults, characterized, respectively, by bias and drift. To model weak faults (and strong faults), we assume that the absolute level b follows a uniform distribution between 20% and 40% (and 60%–90%) of the data amplitude. In addition, the actual level is assigned a random sign, introducing both positive and negative faults in a randomized manner. The fault durations (G and K) are uniformly distributed between five and six consecutive samples. Note that adopting a uniform distribution for both fault level b and fault durations (G and K) aids in assessing the performance of SFDIA without focusing on a specific fault level or length.

For our experimental setup, we consider a total number of $N = 63$ sensors and $M = 3$ local EnKF filters. Each local filter receives a set of 21 sensor measurements. More specifically, the same types of sensor measurements are grouped together and fed as an input to each local: the first local

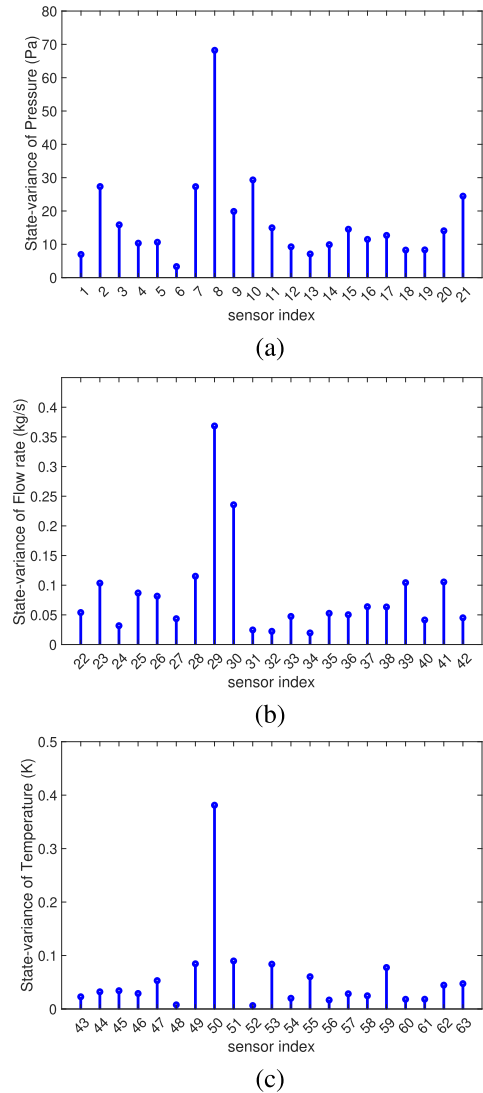


Fig. 4. State variance in the presence of bias fault added simultaneously to three sensors at indices $\ell = 8, 29$, and 50 (all located at spatial node $n = 8$) at time instance $t = 350$ s. (a) State variance of pressure sensors. (b) State variance of flow rate sensors. (c) State variance of temperature sensors.

filter receives 21 pressure measurements, the second local filter receives 21 flow-rate measurements, and the third local filter receives 21 temperature measurements. The ensemble size for the local EnKF filters is chosen as 300, while the conventional EnKF utilizes an ensemble of size 40. This selection aims to optimize the performance of the local filters. The a priori estimate of the local covariance matrix $\mathbf{P}_{i,0|0}$ is chosen as an identity matrix. Furthermore, the standard deviation of the process noise is set 10% lower than the measurement noise. The matrices $\mathbf{Q}_{i,k}$ and $\mathbf{R}_{i,k}$ are considered to be diagonal matrices, with the entries on the main diagonal corresponding to the variances of the process noise and measurement noise, respectively. In the adaptive thresholding approach, the time window is set as $m = 10$ and $m_t = 5$.

We explored the effectiveness of our proposed technique in the presence of three bias and drift faults introduced to the pressure, flow rate, and temperature sensors simultaneously. These faults are associated with indices $\ell = 8, 29$, and 50 , respectively, and span the time period $300 \text{ s} \leq t \leq 500 \text{ s}$. The

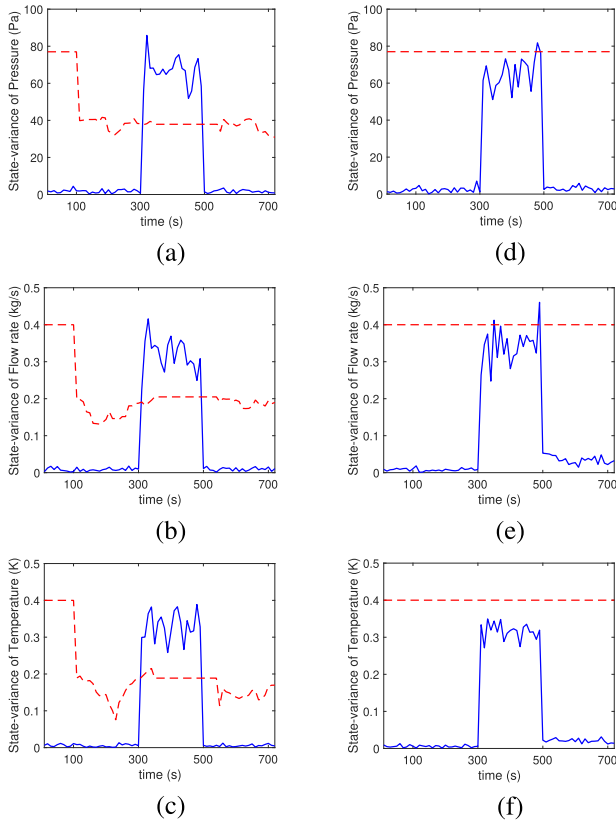


Fig. 5. Comparison between adaptive and fixed thresholding techniques in the presence of weak bias faults corresponding to indices $\ell = 8, 29$, and 50 . (a)–(c) [resp. (d)–(f)] Proposed adaptive (resp. fixed) thresholding technique, where state-variance and threshold values are shown in blue and red, respectively.

actual and estimated state values, determined using our novel MM-SFDIA architecture (outlined in Section III), fusing-UKF (incorporating a single-fault detection and isolation mechanism) [18], and classic EnKF, are depicted in Fig. 3. It is evident from the figure that our proposed MM-SFDIA approach exhibits effective capability in detecting and isolating faulty sensors, thus demonstrating its potentially superior performance over the other techniques. Conversely, alternative methods encounter challenges in accurately estimating the state vector due to their limited ability to detect and isolate sensor faults. Furthermore, Fig. 4 provides a comparison of the state variance $\xi_{l,k}$, as defined in (22), in the context of the bias fault. This comparison pertains to the instances where the faults are attributed to sensor indices $\ell = 8, 29$, and 50 , all situated at spatial node $n = 8$. A clear observation is that the state-variance associated with the aforementioned faulty sensors exhibits significantly elevated values during the time interval $300 \text{ s} \leq t \leq 500 \text{ s}$. This observation confirms the effectiveness of analyzing the state-variance vector values to reliably identify and isolate faulty sensors within the system. Considering weak bias faults affecting sensors at indices $\ell = 8, 29$, and 50 , we contrasted the adaptive thresholding technique, discussed in Section III-D, with the fixed threshold strategy, as depicted in Fig. 5. The results clearly demonstrate the effectiveness of the adaptive thresholding approach in fault detection and isolation.

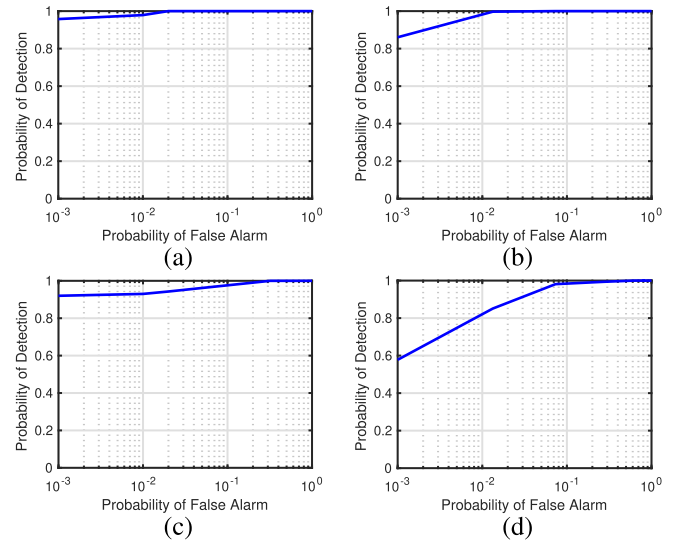


Fig. 6. ROC plots indicating detection performance of MM-SFDIA for three simultaneous faults of distinct types: (a) strong bias (SB), (b) weak bias (WB), (c) strong drift (SD), and (d) weak drift (WD).

Monte Carlo simulations involving 100 runs are conducted using MATLAB² software to obtain the numerical results. The probabilities of detection and false alarm, calculated on a sample-by-sample basis, are chosen as metrics for assessing the detection efficacy of the MM-SFDIA architecture in the presence of multiple sensor faults. To evaluate this performance, receiver operating characteristic (ROC) curves, as depicted in Fig. 6, are generated by varying the adaptive threshold value defined in (27). The findings convincingly highlight the effective fault detection capability of the proposed MM-SFDIA architecture, even while dealing with weak sensor faults. Next, the robustness of the proposed architecture is validated in terms of detection accuracy. In Fig. 7(a), a comparison is presented between detection accuracy and varying fault rates. The results demonstrate that the proposed approach maintains a high level of accuracy, even while dealing with significant faults. Furthermore, the detection accuracy performance is assessed against the varying number of locals in Fig. 7(b). It is evident that the proposed architecture maintains consistent performance with the increasing number of locals. In addition, Fig. 8 depicts the impact of diverse bias levels on detection accuracy. The findings clearly indicate that the proposed framework exhibits high performance even when the bias levels are low.

A comparison between MM-SFDIA and fusing UKF, fusing EnKF and fusing EKF [18], [20], is presented in Table III to evaluate the detection accuracy in a scenario involving a single fault for fixed tuning parameters $r = 13$ and $\lambda = 15$. The outcomes clearly demonstrate that the MM-SFDIA approach exhibits superior performance even in the case of weak faults. A more comprehensive assessment of the proposed architecture in the context of detecting and isolating multiple faults is demonstrated in Fig. 9. The decision outcomes are analyzed over a time interval of 50 samples, focusing on weak bias faults. In this representation, the “o” symbol signifies

²Registered trademark.

TABLE III

CONTRASTING DETECTION ACCURACY (%) OF MM-SFDIA AGAINST FUSING UKF, FUSING EKF, AND FUSING ENKF FOR SINGLE-FAULT CASE, CONSIDERING DIFFERENT TYPES OF FAULT

Fault	Type	MM-SFDIA	Fusing UKF	Fusing EnKF	Fusing EKF
Pressure	Weak Bias	100	100	88.89	45.00
	Weak Drift	100	100	87.50	58.89
Flow rate	Weak Bias	100	100	83.89	97.78
	Weak Drift	85.56	83.89	67.78	92.22
Temperature	Weak Bias	100	97.92	88.25	100
	Weak Drift	99.72	90.83	62.78	93.61

TABLE IV

CONTRASTING COMPUTATION COMPLEXITY OF MM-SFDIA WITH FUSING UKF, FUSING EKF, AND FUSING ENKF, IN TERMS OF EXECUTION TIME AND NUMBER OF LOCALS FOR SINGLE- AND MULTIPLE-FAULT CASE

Method	Total number of sensors	Single Fault		Multiple 3 Faults	
		Execution Time (seconds)	Number of locals	Execution Time (seconds)	Number of locals
Proposed MM-SFDIA	63	3.27s	3	3.29s	3
Fusing UKF	63	27.11s	63	17955.57	41727
Fusing EnKF	63	8.72s	63	5775.54	41727
Fusing EKF	63	29.167s	63	19313.64	41727

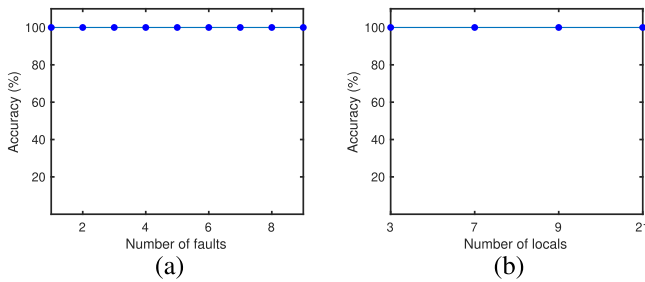


Fig. 7. Detection accuracy performance of MM-SFDIA versus the different numbers of (a) faults and (b) locals (considering three simultaneous weak bias faults).

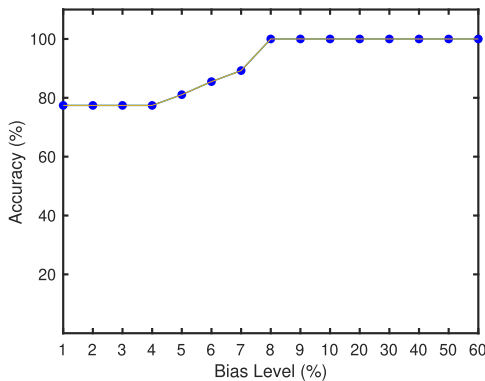


Fig. 8. Detection accuracy of MM-SFDIA versus the bias level considering three simultaneous bias faults.

the actual/true faulty sensors, while “None” indicates the absence of faults within the system. The miss-detected faults are marked with the “*” symbol. In addition, when a fault is detected, the identified faults are indicated with the “+” symbol. A significant observation drawn from Fig. 9 is that the proposed architecture can successfully detect all the faults, leaving no fault undetected and only a few false detections.

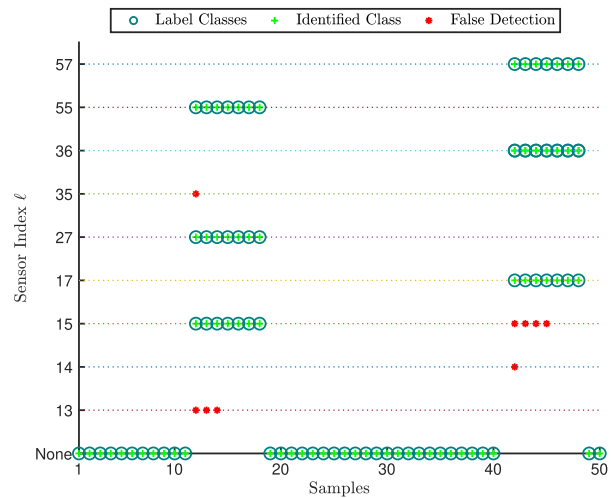


Fig. 9. Fault classification visualization of the proposed architecture.

In addition, an analysis of computation complexity, considering execution time and number of local filters, is presented in Table IV for the proposed MM-SFDIA and various fusing architectures addressing single and multiple faults. The results distinctly demonstrate that the proposed architecture exhibits reduced execution time and employs a lower count of local filters in both single- and multiple-fault scenarios.

V. CONCLUSION

This article presented an innovative model-based architecture for detecting and isolating multiple sensor faults within a natural gas pipeline system experiencing transient flow. The proposed approach leverages a distributed EnKF-based framework, where each local filter is fed with an independent set of measurements for local state estimation. Subsequently, a state-variance vector is computed and compared against an adaptable threshold, enabling the detection of faulty

sensors. These faulty sensor measurements are substituted with corrected measurements obtained via spatial interpolation. Furthermore, a conventional EnKF is employed to generate global estimates using the corrected measurements, which are then shared across all local EnKFs for parameter updation. The simulation results demonstrated the effectiveness of the proposed architecture in detecting and isolating multiple sensor faults simultaneously. Future research will focus on investigating multisensor fault detection in interconnected large-scale wireless sensor networks, exploring alternative distributed filtering methodologies, such as consensus or diffusion.

REFERENCES

- [1] L. Hou, D. Wang, B. Du, X. Qian, and M. Yuan, "Gas concentration detection via multi-channelled air sampling method," *Sensor Rev.*, vol. 37, no. 2, pp. 187–195, Mar. 2017.
- [2] Q. Tan, G. Feng, H. Yuan, G. Su, M. Fu, and Y. Zhu, "Applied research for the gas pipeline installation and the monitoring method for the safety of the adjacent under-ground spaces," *J. Saf. Environ.*, vol. 19, pp. 902–908, 2019.
- [3] H. Darvishi, D. Ciuonzo, E. R. Eide, and P. Salvo Rossi, "Sensor-fault detection, isolation and accommodation for digital twins via modular data-driven architecture," *IEEE Sensors J.*, vol. 21, no. 4, pp. 4827–4838, Feb. 2021.
- [4] H. Darvishi, D. Ciuonzo, and P. Salvo Rossi, "A machine-learning architecture for sensor fault detection, isolation, and accommodation in digital twins," *IEEE Sensors J.*, vol. 23, no. 3, pp. 2522–2538, Feb. 2023.
- [5] W. Junru, W. Tao, and W. Junzheng, "Hybrid modelling for leak detection of long-distance gas transport pipeline," *Insight Non-Destructive Test. Condition Monitor.*, vol. 55, no. 7, pp. 372–381, Jul. 2013.
- [6] S. Shao, R. Yan, Y. Lu, P. Wang, and R. X. Gao, "DCNN-based multi-signal induction motor fault diagnosis," *IEEE Trans. Instrum. Meas.*, vol. 69, no. 6, pp. 2658–2669, Jun. 2020.
- [7] Y. Hu, B. Ping, D. Zeng, Y. Niu, Y. Gao, and D. Zhang, "Research on fault diagnosis of coal mill system based on the simulated typical fault samples," *Measurement*, vol. 161, Sep. 2020, Art. no. 107864.
- [8] J. Yang, F. Zhu, X. Wang, and X. Bu, "Robust sliding-mode observer-based sensor fault estimation, actuator fault detection and isolation for uncertain nonlinear systems," *Int. J. Control, Autom. Syst.*, vol. 13, no. 5, pp. 1037–1046, Oct. 2015.
- [9] J. Wei, G. Dong, and Z. Chen, "Model-based fault diagnosis of lithium-ion battery using strong tracking extended Kalman filter," *Energy Proc.*, vol. 158, pp. 2500–2505, Feb. 2019.
- [10] W. El Sayed, M. Abd El Geliel, and A. Lotfy, "Fault diagnosis of PMSG stator inter-turn fault using extended Kalman filter and unscented Kalman filter," *Energies*, vol. 13, no. 11, p. 2972, Jun. 2020.
- [11] E. Apriliani, L. Hanafi, and C. Imron, "Data assimilation to estimate the water level of river," *J. Phys., Conf. Ser.*, vol. 890, Sep. 2017, Art. no. 012057.
- [12] L. Yan, Y. Zhang, B. Xiao, Y. Xia, and M. Fu, "Fault detection for nonlinear systems with unreliable measurements based on hierarchy cubature Kalman filter," *Can. J. Chem. Eng.*, vol. 96, no. 2, pp. 497–506, Feb. 2018.
- [13] K. Salahshoor, M. Mosallaei, and M. Bayat, "Centralized and decentralized process and sensor fault monitoring using data fusion based on adaptive extended Kalman filter algorithm," *Measurement*, vol. 41, no. 10, pp. 1059–1076, Dec. 2008.
- [14] K. Bader, B. Lussier, and W. Schön, "A fault tolerant architecture for data fusion: A real application of Kalman filters for mobile robot localization," *Robot. Auto. Syst.*, vol. 88, pp. 11–23, Feb. 2017.
- [15] H. Hamadi, B. Lussier, I. Fantoni, and C. Francis, "Data fusion fault tolerant strategy for a quadrotor UAV under sensors and software faults," *ISA Trans.*, vol. 129, pp. 520–539, Oct. 2022.
- [16] K. Geng and N. A. Chulin, "Applications of multi-height sensors data fusion and fault-tolerant Kalman filter in integrated navigation system of UAV," *Proc. Comput. Sci.*, vol. 103, pp. 231–238, 2017.
- [17] F. Lu, Y. Wang, J. Huang, Y. Huang, and X. Qiu, "Fusing unscented Kalman filter for performance monitoring and fault accommodation in gas turbine," *Proc. Inst. Mech. Eng., G, J. Aerosp. Eng.*, vol. 232, no. 3, pp. 556–570, Mar. 2018.
- [18] A. Vafamand, B. Moshiri, and N. Vafamand, "Fusing unscented Kalman filter to detect and isolate sensor faults in DC microgrids with CPLs," *IEEE Trans. Instrum. Meas.*, vol. 71, pp. 1–8, 2022.
- [19] K. Shaheen, A. Chawla, F. E. Uilhoorn, and P. Salvo Rossi, "Model-based sensor-fault detection and isolation in natural-gas pipelines for transient flow," in *Proc. IEEE SENSORS*. IEEE, 2023, pp. 1–4.
- [20] K. Shaheen, A. Chawla, F. E. Uilhoorn, and P. Salvo Rossi, "Sensor-fault detection, isolation and accommodation for natural-gas pipelines under transient flow," *IEEE Trans. Signal Inf. Process. over Netw.*, to be published.
- [21] L. Yan, H. Zhang, X. Dong, Q. Zhou, H. Chen, and C. Tan, "Unscented Kalman-filter-based simultaneous diagnostic scheme for gas-turbine gas path and sensor faults," *Meas. Sci. Technol.*, vol. 32, no. 9, Sep. 2021, Art. no. 095905.
- [22] D. Mori, H. Sugiura, and Y. Hattori, "Adaptive sensor fault detection and isolation using unscented Kalman filter for vehicle positioning," in *Proc. IEEE Intell. Transp. Syst. Conf. (ITSC)*, Oct. 2019, pp. 1298–1304.
- [23] B. Du, Z. Shi, J. Song, H. Wang, and L. Han, "A fault-tolerant data fusion method of MEMS redundant gyro system based on weighted distributed Kalman filtering," *Micromachines*, vol. 10, no. 5, p. 278, Apr. 2019.
- [24] Y. Luo, Y. Liu, W. Yang, J. Zhou, and T. Lv, "Distributed filtering algorithm based on local outlier factor under data integrity attacks," *J. Franklin Inst.*, vol. 360, no. 12, pp. 9290–9306, Aug. 2023.
- [25] N. Sadeghzadeh Nokhodberiz and J. Poshtan, "Belief consensus-based distributed particle filters for fault diagnosis of non-linear distributed systems," *Proc. Inst. Mech. Eng., I, J. Syst. Control Eng.*, vol. 228, no. 3, pp. 123–137, Mar. 2014.
- [26] P. Jin, X. Zhou, C. Wang, J. Huang, W. Zhou, and F. Lu, "A novel distributed Kalman filtering for health state recognition of aero-engine components in networked control systems," *Nonlinear Dyn.*, vol. 111, no. 3, pp. 2571–2589, Feb. 2023.
- [27] M. Saied, A. R. Tabikh, C. Francis, H. Hamadi, and B. Lussier, "An informational approach for fault tolerant data fusion applied to a UAV's attitude, altitude, and position estimation," *IEEE Sensors J.*, vol. 21, no. 24, pp. 27766–27778, Dec. 2021.
- [28] D.-J. Xin, L.-F. Shi, and X. Yu, "Distributed Kalman filter with faulty/reliable sensors based on Wasserstein average consensus," *IEEE Trans. Circuits Syst. II, Exp. Briefs*, vol. 69, no. 4, pp. 2371–2375, Apr. 2022.
- [29] F. E. Uilhoorn, "Comparison of Bayesian estimation methods for modeling flow transients in gas pipelines," *J. Natural Gas Sci. Eng.*, vol. 38, pp. 159–170, Feb. 2017.
- [30] M. W. Zemansky and R. H. Dittman, *Heat and Thermodynamics*. New York, NY, USA: McGraw-Hill, 1943.
- [31] A. R. D. Thorley and C. H. Tiley, "Unsteady and transient flow of compressible fluids in pipelines—A review of theoretical and some experimental studies," *Int. J. Heat Fluid Flow*, vol. 8, no. 1, pp. 3–15, Mar. 1987.
- [32] F. E. Uilhoorn, "A particle filter-based framework for real-time state estimation of a non-linear hyperbolic PDE system describing transient flows in CO₂ pipelines," *Comput. Math. Appl.*, vol. 68, no. 12, pp. 1991–2004, Dec. 2014.
- [33] F. E. Uilhoorn, "Dynamic behaviour of non-isothermal compressible natural gases mixed with hydrogen in pipelines," *Int. J. Hydrogen Energy*, vol. 34, no. 16, pp. 6722–6729, Aug. 2009.
- [34] C. F. Colebrook et al., "Correspondence. turbulent flow in pipes, with particular reference to the transition region between the smooth and rough pipe laws (includes plates)," *J. Inst. Civil Engineers*, vol. 12, no. 8, pp. 393–422, Oct. 1939.
- [35] E. W. Lemmon and R. T. Jacobsen, "Viscosity and thermal conductivity equations for nitrogen, oxygen, argon, and air," *Int. J. Thermophys.*, vol. 25, no. 1, pp. 21–69, Jan. 2004.
- [36] J. F. Helgaker, A. Oosterkamp, L. I. Langelandsvik, and T. Ytrehus, "Validation of 1D flow model for high pressure offshore natural gas pipelines," *J. Natural Gas Sci. Eng.*, vol. 16, pp. 44–56, Jan. 2014.
- [37] W. E. Schiesser, *The Numerical Method of Lines: Integration of Partial Differential Equations*. Amsterdam, The Netherlands: Elsevier, 2012.
- [38] R. Courant, "Über die partiellen Differenzgleichungen der mathematischen Physik," *Mathematische Annalen*, vol. 100, no. 1, pp. 32–74, Dec. 1928.
- [39] R. Olfati-Saber, "Distributed Kalman filtering for sensor networks," in *Proc. 46th IEEE Conf. Decis. Control*, 2007, pp. 5492–5498.
- [40] K. Patan, *Artificial Neural Networks for the Modelling and Fault Diagnosis of Technical Processes*. Cham, Switzerland: Springer, 2008.

- [41] S. Amirkhani, A. Chaibakhsh, and A. Ghaffari, "Nonlinear robust fault diagnosis of power plant gas turbine using Monte Carlo-based adaptive threshold approach," *ISA Trans.*, vol. 100, pp. 171–184, May 2020.



Khadija Shaheen (Member, IEEE) received the M.Sc. degree in electrical engineering with specialization in digital systems and signal processing (DSSP) from the School of Electrical Engineering and Computer Science (SEECs), National University of Sciences and Technology (NUST), Islamabad, Pakistan, in 2021. She is currently pursuing the Ph.D. degree in electronics with the Department Electronic Systems, Norwegian University of Science and Technology (NTNU), Trondheim, Norway.

Her research interests include sensor validation, machine learning, and digital signal processing.



Apoorva Chawla (Member, IEEE) received the B.Tech. degree in electronics and communication engineering from Gautam Buddha Technical University, Lucknow, India, in 2012, and the M.Tech. and Ph.D. degrees in electrical engineering from the Indian Institute of Technology Kanpur, Kanpur, India, in 2022.

She is currently a Postdoctoral Researcher with the Department of Electronic Systems, Norwegian University of Science and Technology (NTNU), Trondheim, Norway. Her research

interests include sensor validation, the Internet of Things, distributed detection, wireless communication, and signal processing.

Dr. Chawla was awarded the TCS Research Fellowship for pursuing graduate studies at the Indian Institute of Technology Kanpur. In 2019, she was selected as one of the finalists for the Qualcomm Innovation Fellowship by Qualcomm, India.



Ferdinand Evert Uilhoorn received the B.Sc. and M.Sc. degrees in mechanical and systems engineering from Polytechnic Groningen, Groningen, The Netherlands, and the Delft University of Technology, Delft, The Netherlands, in 1997 and 2002, respectively, and the Ph.D. (cum laude) and D.Sc. degrees in gas engineering from the Warsaw University of Technology, Warsaw, Poland, in 2007 and 2017, respectively.

He is currently an Associate Professor with the Gas Engineering Group, Warsaw University of Technology. His research interests include single- and multiphase flow modeling, numerical methods, and data assimilation, with a focus on pipeline systems.



Pierluigi Salvo Rossi (Senior Member, IEEE) was born in Naples, Italy, in 1977. He received the Dr.Eng. (summa cum laude) degree in telecommunications engineering and the Ph.D. degree in computer engineering from the University of Naples "Federico II," Naples, in 2002 and 2005, respectively.

He worked with the University of Naples "Federico II"; the Second University of Naples, Naples; the Norwegian University of Science and Technology (NTNU), Trondheim, Norway; and Kongsberg Digital AS, Horten, Norway. He held visiting appointments with Drexel University, Philadelphia, PA, USA; Lund University, Lund, Sweden; NTNU; and Uppsala University, Uppsala, Sweden. He is currently a Full Professor and the Deputy Head with the Department of Electronic Systems, NTNU. He is also a part-time Research Scientist with the Department of Gas Technology, SINTEF Energy Research, Trondheim. His research interests fall within the areas of communication theory, data fusion, machine learning, and signal processing.

Prof. Salvo Rossi was awarded as an Exemplary Senior Editor of the IEEE COMMUNICATIONS LETTERS in 2018. He is (or has been) on the Editorial Board of the IEEE SENSORS JOURNAL, the IEEE OPEN JOURNAL OF THE COMMUNICATIONS SOCIETY, IEEE TRANSACTIONS ON SIGNAL AND INFORMATION PROCESSING OVER NETWORKS, the IEEE COMMUNICATIONS LETTERS, and IEEE TRANSACTIONS ON WIRELESS COMMUNICATIONS.